The intramembrane COOH-terminal domain of PRRT2 regulates voltage-dependent Na$^+$ channels

Francesca Franchi[1,2], Antonella Marte[2,3], Beatrice Corradi[1,2], Bruno Sterlini[2], Giulio Alberini[1,3], Alessandra Romei[1], Antonio De Fusco[1], Alexander Vogel[1], Luca Maragliano[1,4], Pietro Baldelli[2,3], Anna Corradi[2,3], Pierluigi Valente[2,3], and Fabio Benfenati[1,3,*]

From the [1]Center for Synaptic Neuroscience and Technology, Istituto Italiano di Tecnologia, Genova, Italy; [2]Department of Experimental Medicine, University of Genova, Genova, Italy; [3]IRCCS, Ospedale Policlinico San Martino, Genova, Italy; [4]Department of Life and Environmental Sciences, Polytechnic University of Marche, Ancona, Italy

Reviewed by members of the JBC Editorial Board. Edited by Mike Shipston

Proline-rich transmembrane protein 2 (*PRRT2*) is the single causative gene for pleiotropic paroxysmal syndromes, including epilepsy, kinesigenic dyskinesia, episodic ataxia, and migraine. PRRT2 is a neuron-specific type-2 membrane protein with a COOH-terminal intramembrane domain and a long proline-rich NH$_2$-terminal cytoplasmic region. A large array of experimental data indicates that PRRT2 is a neuron stability gene that negatively controls intrinsic excitability by regulating surface membrane localization and biophysical properties of voltage-dependent Na$^+$ channels Nav1.2 and Nav1.6, but not Nav1.1. To further investigate the regulatory role of PRRT2, we studied the structural features of this membrane protein with molecular dynamics simulations, and its structure-function relationships with Nav1.2 channels by biochemical and electrophysiological techniques. We found that the intramembrane COOH-terminal region maintains a stable conformation over time, with the first transmembrane domain forming a helix–loop–helix motif within the bilayer. The unstructured NH$_2$-terminal cytoplasmic region bound to the Nav1.2 better than the isolated COOH-terminal intramembrane domain, mimicking full-length PRRT2, while the COOH-terminal intramembrane domain was able to modulate Na$^+$ current and channel biophysical properties, still maintaining the striking specificity for Nav1.2 *versus* Nav1.1. channels. The results identify PRRT2 as a dual-domain protein in which the NH$_2$-terminal cytoplasmic region acts as a binding antenna for Na$^+$ channels, while the COOH-terminal membrane domain regulates channel exposure on the membrane and its biophysical properties.

Proline-rich transmembrane protein 2 (*PRRT2*) is the causative gene for a clinical-genetic spectrum of heterogeneous paroxysmal neurological disorders (1, 2). *PRRT2* mutations account for a large fraction of cases of familial benign infantile epilepsy, paroxysmal kinesigenic dyskinesia (PKD) and PKD with infantile convulsions (PKD/IC) and, conversely, 95% of PRRT2 patients have a diagnosis within the benign familial infantile epilepsy PKD/IC-PKD spectrum. In addition, 5% of PRRT2 patients display other disorders, such as episodic ataxia, hemiplegic migraine, developmental delay, and intellectual disability (3–8). To date, about 1500 patients with 70 different mutations have been reported, 75% of whom carrying the same frameshift mutation (c.649dupC). About 75% of all reported *PRRT2* mutations involve insertion of a precocious stop codon, leading to unstable mRNA and/or a truncated protein that is degraded, while some missense mutations may lead to PRRT2 mislocalization (9–12). Patients bearing homozygous or compound heterozygous mutations in *PRRT2* show a severe encephalopathic phenotype, with paroxysmal dyskinesias, unusually prolonged ataxia attacks, seizures, and intellectual disability (13–15).

A large body of experimental data have contributed to the understanding of PRRT2 function and pathogenesis of paroxysmal disorders associated with loss-of-function mutations in *PRRT2*, that has been described as a network stability gene (16, 17). We and other groups have found that genetic deletion of the *PRRT2* gene in the mouse (PRRT2KO) mimics the human pathology and displays network hyperexcitability particularly in brain areas where PRRT2 is highly expressed, such as the cerebellum and the hippocampus (18–25). Physiological levels of PRRT2 seem to be necessary to maintain a normal level of network activity, so that an overexpression of PRRT2, occurring in the 16p11.2 duplication, is also associated with neuropsychiatric disorders including epilepsy (26). PRRT2 is composed of a large proline-rich intracellular NH$_2$-terminal domain and two hydrophobic segments of which the second one spans the plasma membrane, whereas the first one forms a helix-loop-helix structure within the inner leaflet of the membrane without crossing it completely (27). PRRT2 is enriched in the axon and nerve terminals and its silencing impairs synchronous release by decreasing the Ca^{2+} sensitivity of neurotransmitter release and thereby greatly increasing synaptic facilitation (21, 28–30).

In addition to the synaptic dysfunction, a major contribution to hyperexcitability is due to the increased Na$^+$ current density observed in PRRT2KO mice and induced pluripotent stem cell-derived human neurons from homozygous patients (21, 31).

Interestingly, PRRT2 is a physiological inhibitor of Nav1.2/Nav1.6 which predominantly sustain the firing activity of excitatory neurons, while not affecting Nav1.1 channels that play a central role in firing of inhibitory neurons (32, 33). This way, the loss-of-function of PRRT2 unleashes the constraint on excitability of excitatory neurons, generating an excitatory/inhibitory unbalance (16, 18, 21, 31). In heterologous systems, PRRT2 acts as a negative modulator of Nav1.2/1.6 channels by decreasing their targeting to the plasma membrane, shifting the inactivation curve toward more negative voltages and impairing channel recovery after inactivation (31). Many of these effects are opposite to the actions of Nav β-subunits, suggesting that they may result from an antagonistic interaction between PRRT2 and β-subunits. However, no detectable molecular and/or functional interactions were found (34). These findings, supported by the proven efficacy of Na$^+$ channel antagonists in PRRT2 patients and mutant mice (35–37), indicate that PRRT2 directly interacts with the Nav α-subunits.

Here, based on the membrane topology of PRRT2, we studied the conformational features of the bilayer-spanning region with microsecond-time scale molecular dynamics (MD) simulations to validate and further refine our previous structural model (27). These simulations revealed that PRRT2 maintains a stable conformation within the membrane, characterized by the presence of a helix-loop-helix motif, a short cytoplasmic loop, and a transmembrane helix. We then investigated the structure-function relationships of PRRT2 with Nav1.2 channels by biochemical and electrophysiological techniques. We found that both the NH$_2$-terminal and COOH-terminal regions of PRRT2 bind Nav1.2, while the latter intramembrane domain is responsible for the modulation the membrane targeting and biophysical properties of Nav1.2 channels. Both PRRT2 regions did not significantly interact with Nav1.1. channels. The results identify PRRT2 as a multidomain protein in which the NH$_2$-terminal cytoplasmic region binds the Nav1.2 channel but is unable to modulate it, while the COOH-terminal transmembrane region is responsible for the modulation of the channel fate and properties.

Results

PRRT2 deletion mutants are expressed and targeted to the plasma membrane in Hek293 cells

Given the specific interaction with Nav1.2/1.6, but not with Nav1.1, channels, it was of interest to investigate whether the transmembrane COOH-terminal region or the cytosolic NH$_2$-terminal region of the molecule was responsible for the specific interaction. To this aim, we generated two PRRT2 deletion mutants alternatively lacking the two regions and fused to a HA reporter sequence, namely: PRRT2ΔC-HA, a chimeric protein composed of the NH$_2$-terminal cytoplasmic PRRT2 domain anchored to the membrane by the transmembrane domain of the structurally homologous protein interferon-induced transmembrane protein 1 (IFITM1; (38)) and PRRT2ΔN-HA composed of the COOH-terminal transmembrane domain of PRRT2 including the short cytoplasmic loop (Fig. 1A). Full-length PRRT2-HA or either mutant

construct was then transfected in naïve and Hek293 clones expressing Nav1.2 channels (Figs. 1B and S1). All mutants were correctly expressed and did not interfere with Nav1.2 expression (Fig. S1). Moreover, the HA immunoreactivity of all three constructs was found in association with Nav1.2 channels stained with pan-Nav antibodies (Fig. 1B). Live staining of nonpermeabilized Hek-Nav1.2 cells with anti-HA antibodies confirmed the membrane targeting of the PRRT2 variants, as deduced from the staining of the surface-exposed COOH-terminal HA (Fig. 1C).

Refinement of the structure of the PRRT2 COOH-terminal region by MD simulations

We previously reported (27) that PRRT2 is an atypical dyspanin, presenting a long and unstructured intracellular NH$_2$-terminal region (residues M1 to R266), a first intramembrane domain (TM1a-b, residues D267 to Q300, intervals according to the OPM server https://opm.phar.umich.edu/) that bends with a short hinge including two proline residues (P279 and P282) to form a helix-loop-helix structure; a full membrane-spanning domain (TM2, residues V303 to G337), and a minimal extracellular COOH-terminal, V338 to K340 (Fig. 2A). In our structural model, the C terminus of TM1b (S294 to Q300) and the N terminus of TM2 (V303 to R311) are in the cytosol and, opposite to what obtained in a previous bioinformatic analysis (1), they are connected by only two residues (G301 and D302).

Here, we refined our transmembrane domain model by performing two distinct, 1 μs-long, MD simulations, one using the standard approach with 2 fs timestep, and one with hydrogen mass repartitioning and 4 fs timestep. These simulations demonstrated a high degree of structural stability for the transmembrane PRRT2 segment: the α-carbon PRRT2 root-mean-square deviation from the starting structure was stationary in both replicas after 250 ns (Fig. 2B), and the evolution of the cross-distances between A272, S294, and A313, belonging to the three distinct intramembrane stretches, remained stable over time (Figs. 2, C and D and S2). These results support the previously proposed model of PRRT2, which was based on much shorter simulation times (50 ns; 27). We also compared our transmembrane model, originally obtained by Robetta, with two additional ones predicted by the AlphaFold2 (39) and ESMFold (40) algorithms and found strong structural similarities between them (Fig. 2E). Indeed, the AlphaFold2 and ESMFold models have the same characteristic sequence of secondary structure elements as Robetta's, with almost any differences in their span and relative position between the three conformations. The root-mean-square deviations of the AlphaFold2 and ESMFold models from the Robetta model are 6.62 and 3.46 Å, respectively, values in line with those observed along the simulated trajectory of the latter.

Both the NH$_2$- and COOH-terminal regions of PRRT2 bind Nav1.2 channels

To ascertain which region of PRRT2 directly interacts with the Nav1.2 α-subunit and the basis for its specificity, we
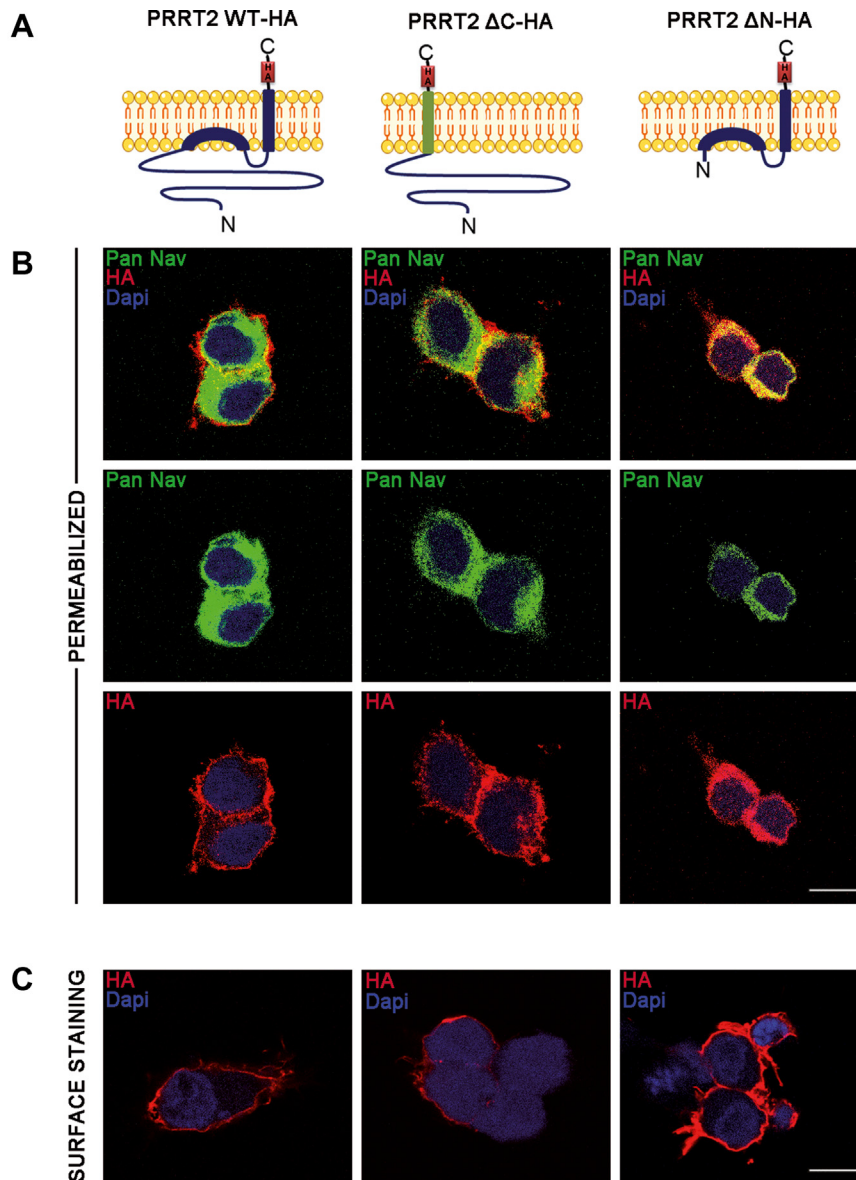
Figure 1. Generation and characterization of the PRRT2 deletion mutants. *A*, schematics of the PRRT2 domain constructs. PRRT2 WT-HA is the entire protein (*violet*). PRRT2 ΔC-HA is a chimeric protein composed of the cytoplasmic PRRT2 (*violet*) domain anchored to the membrane by the transmembrane domain of IFITM1 (*green*). PRRT2 ΔN-HA is composed of the transmembrane domain of PRRT2. *B*, Hek- Nav1.2 cells transfected with (from *left to right*) PRRT2-HA, PRRT2ΔC-HA, and PRRT2ΔN-HA were permeabilized and subsequently labeled for anti-HA and pan-Nav antibodies, respectively, with nuclei marked with DAPI. The individual HA and pan-Nav staining are shown together with the respective merge images (*top row*). *C*, Hek-Nav cells transfected with PRRT2-HA, PRRT2ΔC-HA, and PRRT2ΔN-HA were surface-labeled with anti-HA to stain the membrane-exposed domains of the proteins. Scale bar, 10 μm. IFITM1, interferon-induced transmembrane protein 1; *PRRT2*, proline-rich transmembrane protein 2.

performed affinity binding assays by challenging HA-tagged PRRT2 variants purified from naïve Hek293 cells with extracts of Hek293 clones stably expressing either Nav1.2 or Nav1.1 α-subunits in the absence of β-subunits. After incubation, PRRT2-HA variants were pulled down with anti-HA beads and the associated Nav channels identified by Western blotting with anti-pan-Nav antibodies (Fig. 3A). Full-length PRRT2 efficiently pulled down Nav1.2, but not Nav1.1, α-subunits, as previously described (31). The Nav1.2 binding activity was retained when either PRRT2ΔN (COOH-terminal PRRT2) or PRRT2ΔC (NH2-terminal PRRT2) were assayed but to a different extent. In fact, while PRRT2ΔC bound Nav1.2 to the same extent of full-length PRRT2, PRRT2ΔN exhibited only about 50% of full-length PRRT2 binding. However, both deletion mutants strictly preserved their binding specificity for Nav1.2 α-subunits, and their binding to the Nav1.1 α-subunit was negligible (Fig. 3B).

The PRRT2 COOH-terminal region decreases the Na+ current density in Na$_V$1.2-expressing cells

We next investigated the ability of the PRRT2 deletion mutant to mimic the effects of full-length PRRT2 in inhibiting the transient Na+ current in Nav1.2-expressing Hek293 cells analyzed by whole-cell patch-clamp recordings (Fig. 4A). HA-tagged PRRT2 variants were expressed to the same extent in
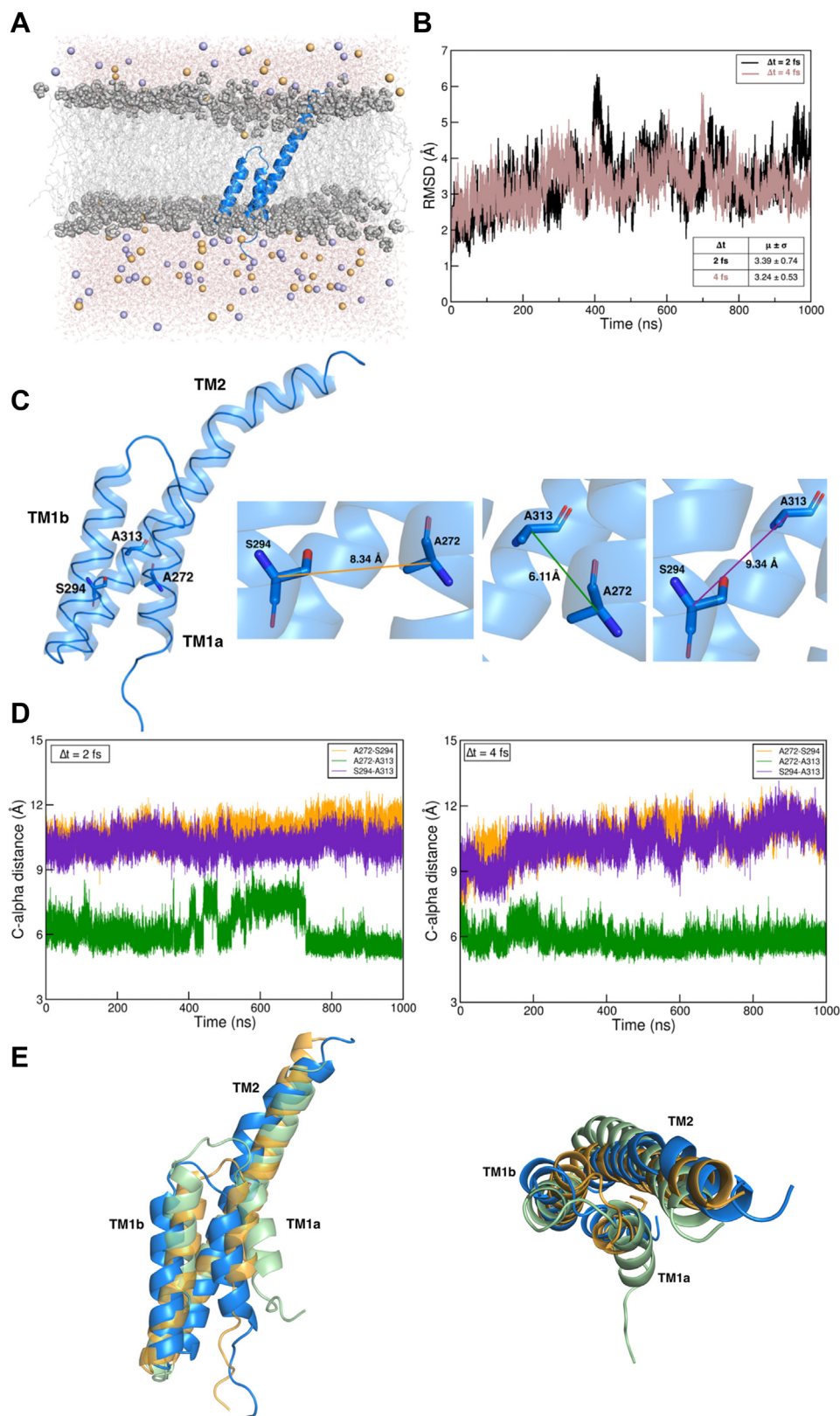
Figure 2. Molecular modeling of the PRRT2 transmembrane segment. *A*, snapshot of the simulated system extracted from a trajectory; PRRT2 is represented in *blue cartoon*, phospholipids heads and tails as *gray spheres and sticks*, respectively, water molecules as *red* and *white sticks*, and sodium and chloride ions as *orange and purple spheres*, respectively. *B*, alpha-carbon RMSD of PRRT2 calculated along the two simulated trajectories at different timesteps (Δt); average values and S.D. are indicated. *C*, cartoon representation of the PRRT2 transmembrane domain; residues involved in the calculated cross-distances are represented as *sticks*; the values reported are those at the beginning of the simulations. *D*, cross-distances evolution for PRRT2 trajectories. *E*, lateral and extracellular views of Robetta (*blue*) AlphaFold2 (*green*), and ESMFold (*orange*) PRRT2 models, superimposed *via* PyMOL. *PRRT2*, proline-rich transmembrane protein 2.
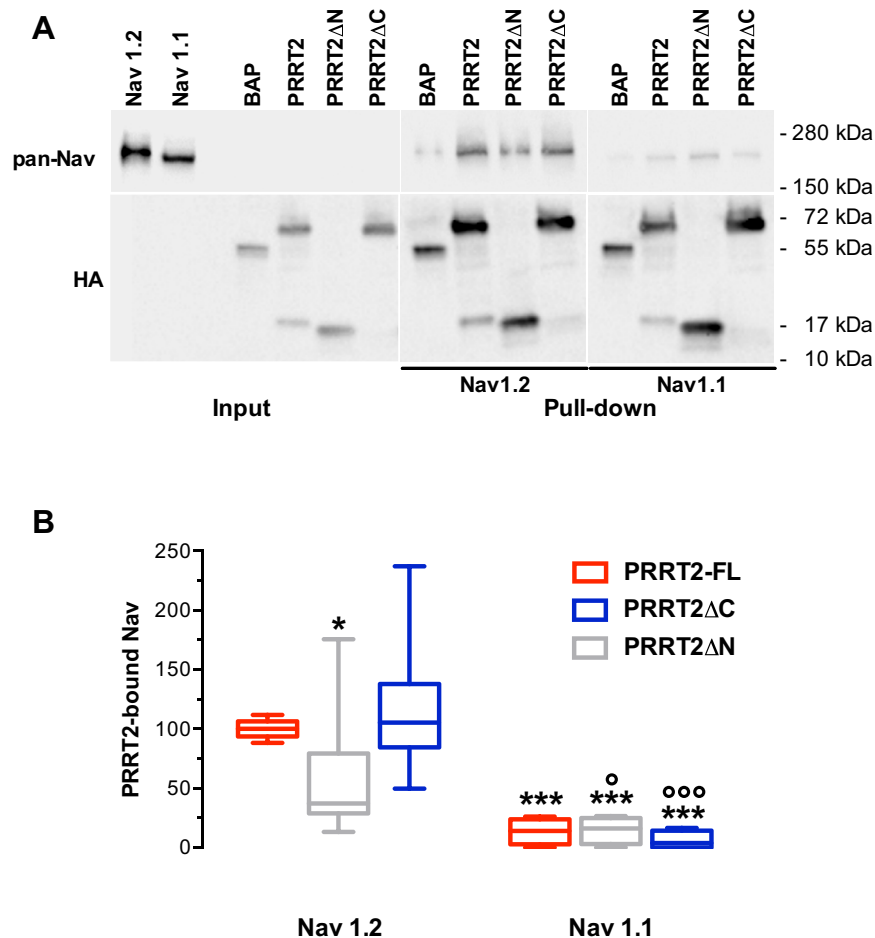
Figure 3. Binding of PRRT2 deletion mutants to Nav1.2 and Nav1.1 channels. *A*, representative immunoblot of co-immunoprecipitation of PRRT2 variants. HA-tagged bacterial alkaline phosphatase (BAP), HA-tagged full-length PRRT2 (PRRT2-FL), or its deletion mutants PRRT2ΔN and PRRT2ΔC were expressed in naive Hek293 cells and purified by HA-immunoprecipitation. The extract of Hek293 stable clones expressing either human Nav1.2 or human Nav1.1 was added to the HA-immunoprecipitated BAP, PRRT2, or PRRT2 deletion mutants. Cell lysates (INPUT, 10 μg protein) and samples immunoprecipitated by anti-HA beads were analyzed by Western blotting with pan-Nav and HA antibodies. Molecular mass standards are reported on the right. The representative blots were cut from the same gel. *B*, quantification of the immunoreactive signals in PRRT2-HA immunoprecipitates. Box plots of n = 6 and 4 independent experiments for Hek-Nav1.2 and Hek-Nav1.1, respectively. *$p < 0.05$, ***$p < 0.001$ *versus* full-length PRRT2; °$p < 0.05$, °°°$p < 0.001$ Nav1.1 *versus* Nav1.2 for each PRRT2 variant. Two-way ANOVA/Fisher's tests. *PRRT2*, proline-rich transmembrane protein 2.

Hek-Nav1.2 cells (Fig. S3). As previously reported (31, 34), full-length PRRT2 significantly decreased the Na⁺ current density with respect to cells transfected with the empty vector (MOCK). Interestingly, the effects of PRRT2ΔN were indistinguishable from those of full-length PRRT2, while PRRT2ΔC was substantially ineffective (Fig. 4*B*). The modulation of the Na⁺ current density by full-length PRRT2 and PRRT2ΔN were highly significant in the −20 to 0 mV range (Fig. 4*C*). However, no significant voltage shift of the current density/voltage (J/V) curves was observed (Fig. 4*B*).

The PRRT2 COOH-terminal region modulates the biophysical properties of Nav1.2 channels

In addition to a constraint on the transient Na⁺ current, the expression of PRRT2 also negatively modulated intrinsic excitability by affecting the inactivation and recovery from inactivation of Nav1.2/1.6 channels (31). Here, we investigated the activity of the NH₂- and COOH-terminal regions of PRRT2 by challenging its deletion mutants with Hek293 cells

stably expressing Nav1.2. The activation dynamics of the Nav1.2 α-subunit, that is heavily modulated by the β-subunits (41), is not significantly affected by either the expression of full-length PRRT2 or its deletion mutants with respect to MOCK-transfected cells in terms of voltage sensitivity (slope) and voltage of half-activation ($V_{0.5}$; Fig. 5*A*). On the contrary, full-length PRRT2 induced a significant left shift of the steady-state inactivation curve of Nav1.2 by significantly decreasing the voltage of half-inactivation toward more negative values with respect to MOCK-transfected cells (Fig. 5*B*). The same effect, with similar magnitude, was triggered by the expression of the PRRT2ΔN mutant, while the expression of the PRRT2ΔC mutant was totally ineffective (Fig. 5*B*). Similar effects were observed on the Nav1.2 recovery from inactivation (Fig. 6*A*). The COOH-terminal region of PRRT2 fully recapitulated the significant decrease in the plateau of recovery induced by full-length PRRT2, while the cytosolic NH₂-terminal region of PRRT2 was ineffective (Fig. 5*B*).
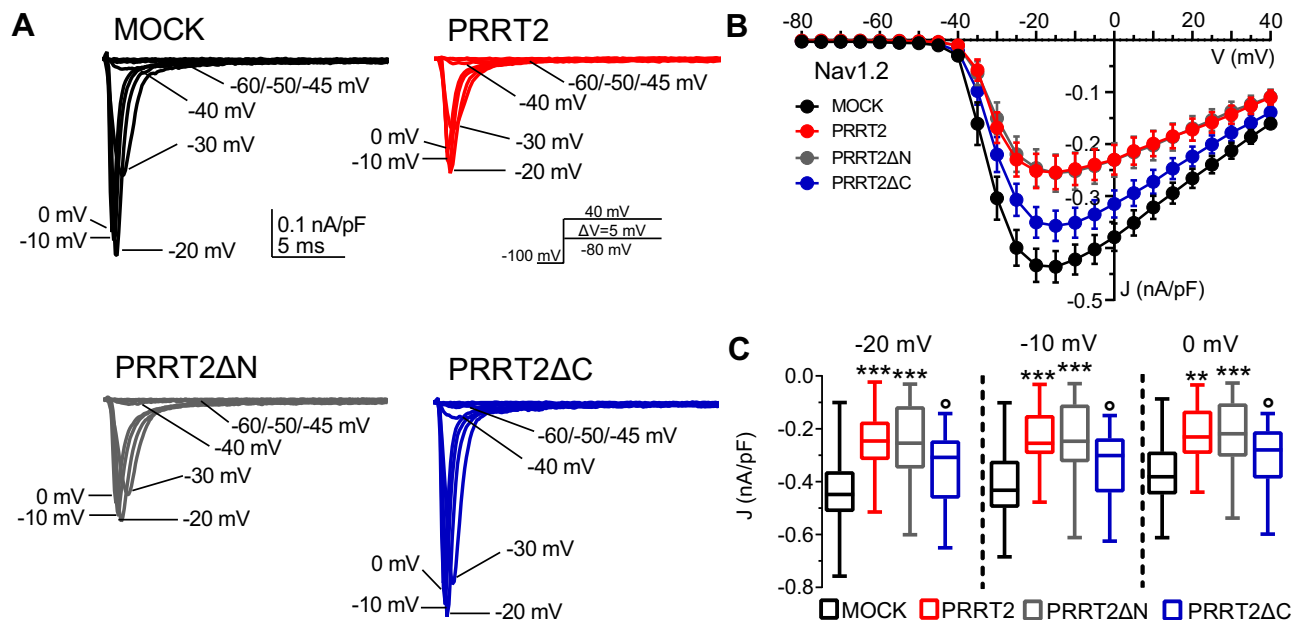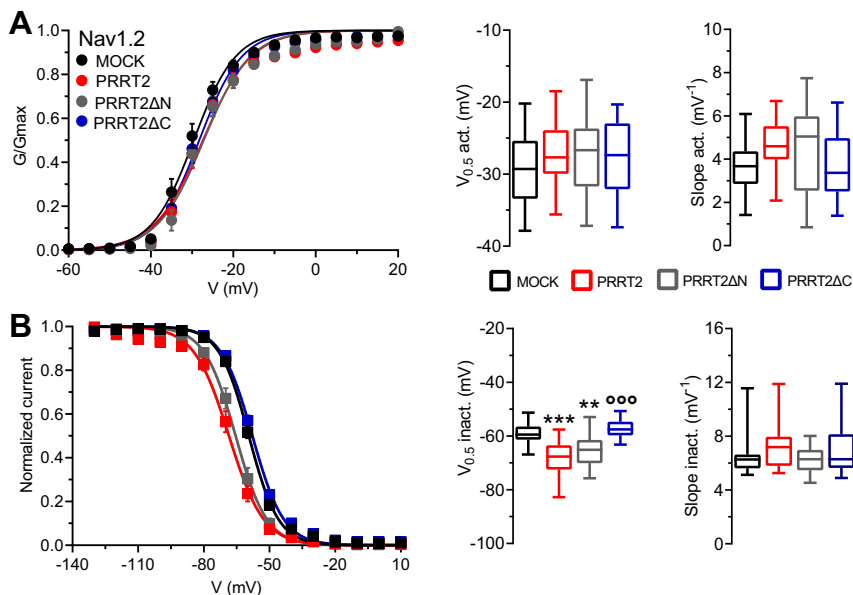
Figure 4. Effects of PRRT2 deletion mutants on the transient Nav1.2 current. *A*, representative whole-cell Na$^+$ currents recorded in Hek293 cells stably expressing Nav1.2 α-subunits and transiently transfected with empty vector (MOCK, *black*), full-length PRRT2 (*red*), PRRT2ΔN (*gray*), and PRRT2ΔC (*blue*). Currents were elicited by a protocol (*inset*) consisting of 5-mV depolarization steps from −80 to 40 mV from a holding potential of −100 mV. For clarity, the first 20 ms of the 100-ms steps for eight representative traces per condition are plotted. *B*, current density (*J*) versus voltage (*V*) relationship for the four experimental conditions. *C*, box plots of *J* values at three representative voltages (−20/-10/0 mV). MOCK, n = 24; full-length PRRT2, n = 15; PRRT2ΔN, n = 19; PRRT2ΔC, n = 21. **$p < 0.01$, ***$p < 0.001$ *versus* MOCK; °$p < 0.05$ *versus* full-length PRRT2. One-way ANOVA/uncorrected Fisher's LSD test. *PRRT2*, proline-rich transmembrane protein 2.

Both the NH$_2$- and COOH-terminal regions of PRRT2 do not interact with Nav1.1 channels

We next investigated whether the functional specificity of full-length PRRT2 for Nav subtypes was preserved to some

extent in its deletion mutants, as suggested by co-immunoprecipitation experiments. Both full-length PRRT2 and well as its PRRT2ΔN and PRRT2ΔC mutants did not significantly affect the density of the transient Na$^+$ currents

Figure 5. Effects of PRRT2 deletion mutants on the activation and inactivation kinetics of Nav1.2 channels. Hek293 cells stably expressing Nav1.2 α-subunits were transiently transfected with empty vector (MOCK, *black*), full-length PRRT2 (*red*), PRRT2ΔN (*gray*), and PRRT2ΔC (*blue*). *A*, *Left:* Voltage-dependence of activation. The lines are the best-fitted Boltzmann curves. *Right:* Box plots of the half-maximal voltage of activation (V$_{0.5}$) and slope (MOCK, n = 24; full-length PRRT2, n = 15; PRRT2ΔN, n = 19; PRRT2ΔC, n = 21). *B*, *Left:* Steady-state inactivation curves. The lines are the best-fitted Boltzmann curves. *Right:* Means (±SEM) values of the half-maximal voltages for inactivation (V$_{0.5}$ inact.) and slopes (MOCK, n = 20; full-length PRRT2, n = 18; PRRT2ΔN, n = 15; PRRT2ΔC, n = 21). **$p < 0.01$, ***$p < 0.001$ *versus* MOCK; °°°$p < 0.001$ *versus* full-length PRRT2. One-way ANOVA/Dunnett's test. *PRRT2*, proline-rich transmembrane protein 2.
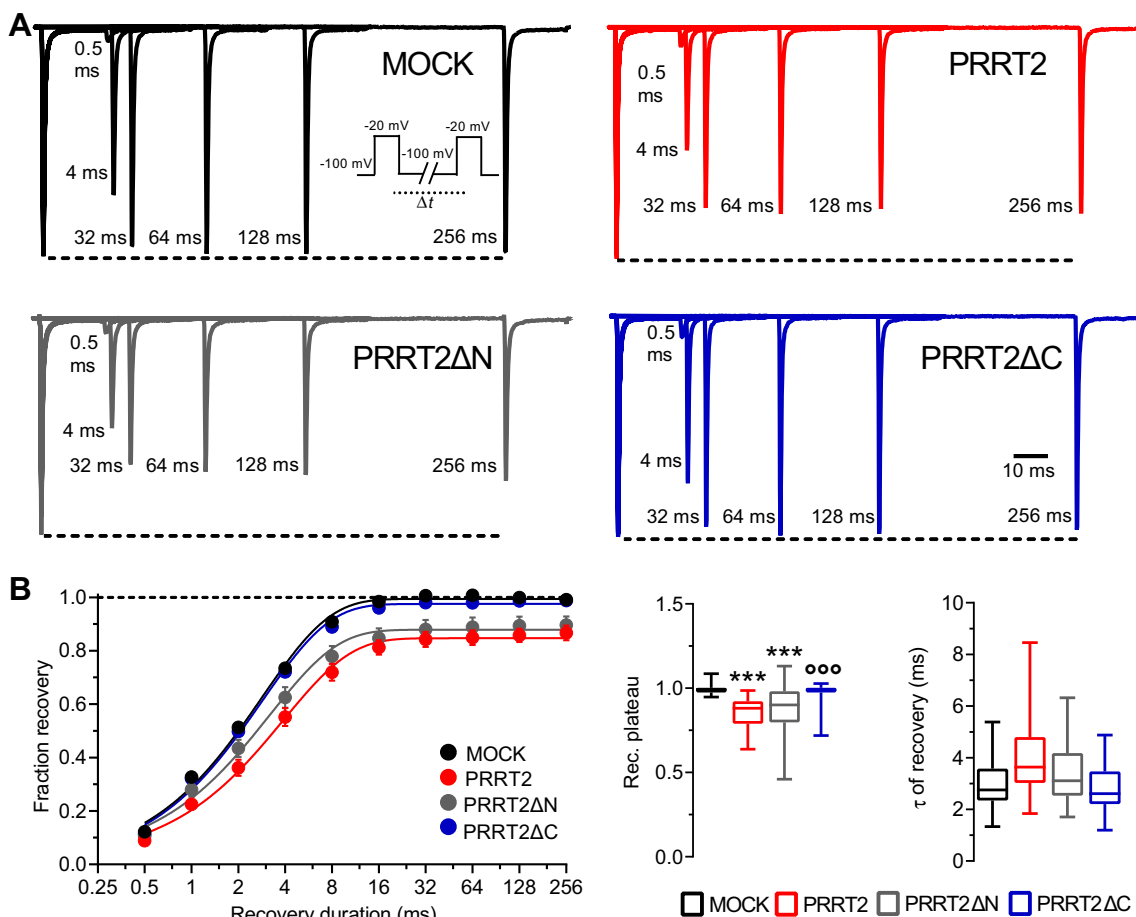
Figure 6. Effects of PRRT2 deletion mutants on the recovery from inactivation of Nav1.2 channels. *A*, representative traces showing current recovery from inactivation for all the experimental conditions. Recordings were obtained prepulsing cells to −20 mV for 20 ms to inactivate Na⁺ currents and then coming back to a recovery potential of −100 mV for increasing durations before the repetition of test pulse to −20 mV. For clarity, 6 of the 9 time-intervals are shown. *B, left:* the time courses of the recovery from inactivation of peak currents at −20 mV are plotted on a semi-logarithmic scale for the four experimental conditions. *Right:* Box plots of τ and plateau of recovery estimated from one-phase decay fit to the data (MOCK, n = 24; full-length PRRT2, n =16; PRRT2ΔN, n = 18; PRRT2ΔC, n = 21). ***$p < 0.001$ *versus* MOCK; °°°$p < 0.001$ *versus* full-length PRRT2. Kruskal–Wallis/Dunn's tests. *PRRT2*, proline-rich transmembrane protein 2.

nor its voltage dependence with respect to MOCK-transfected Hek293 cells stably expressing Nav1.1 channels (Fig. 7A). Similarly, both full-length PRRT2 and its deletion mutants were totally ineffective in altering the parameters of activation (Fig. 7B and C), steady-state inactivation (Fig. 7, D and E), and recovery from inactivation (Fig. 7F) curves of Nav1.1 channels.

Discussion

Given the common paroxysmal character of the pleiotropic diseases linked to PRRT2 loss-of-function (3, 6–8), the lack of negative modulation of Na⁺ channels can be proposed as the key pathogenetic mechanism, in addition to the excitatory/inhibitory imbalance in short-term plasticity (21, 31). The interactions of PRRT2 with Na⁺ channels not only provide a basis for the pathogenesis of the PRRT2-linked paroxysmal manifestations, but also indicate that PRRT2 could be a "*chameleon-like*", multifunctional protein controlling network stability (16, 17). A strong support to the pathogenic role of the disruption of PRRT2/Nav interactions is provided by the efficacy of Na⁺ channel blockers in the therapy of PRRT2-linked

diseases (35–37). Thus, the PRRT2/Nav interaction is worth investigating to clarify the pathogenesis of the diseases and the genotype-phenotype relationships, as well as to develop new targeted therapies.

A fundamental topic to clarify is the PRRT2 structure-function relationships, *i.e.*, which are the protein domains responsible for the interaction with Nav1.2/1.6 and for affecting their turnover between the plasma membrane and the intracellular stores and their biophysical properties. PRRT2 displays two distinct regions, an NH₂-terminal unstructured proline-rich region and an intramembrane COOH-terminal region forming a helix-loop-helix a very short cytosolic loop and a transmembrane segment ending with a COOH-terminal tripeptide ((27); this paper).

In the absence of an experimentally determined structure for PRRT2, we previously proposed an atom-detailed model of its 79 amino acid-long intramembrane region, generated using Robetta and refined with short MD simulations (27). Here, to further validate the model, we extended the simulations to the µs-time scale, revealing that the protein maintained a stable conformation with all the distinctive features of the model. We
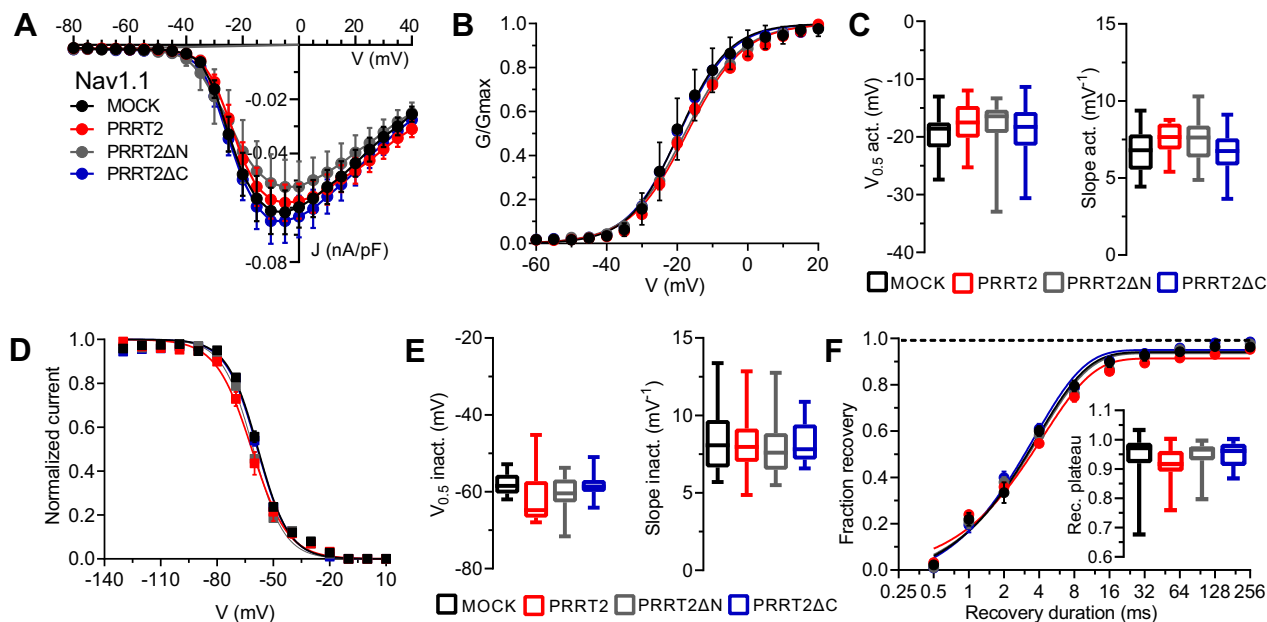
Figure 7. PRRT2 deletion mutants are ineffective on the transient current and biophysical properties of Nav1.1 channels. Hek293 cells stably expressing Nav1.1 α-subunits were transiently transfected with empty vector (MOCK, *black*), full-length PRRT2 (*red*), PRRT2ΔN (*gray*), and PRRT2ΔC (*blue*). *A*, current density (J) *versus* voltage (V) relationship for the four experimental conditions, *B*, voltage-dependence of activation. The lines are the best-fitted Boltzmann curves. *C*, box plots of the half-maximal voltage of activation ($V_{0.5}$) and slope (MOCK, n = 21; full-length PRRT2, n = 19; PRRT2ΔN, n = 18; PRRT2ΔC, n = 23). *D*, steady-state inactivation curves. The lines are the best-fitted Boltzmann curves. *E*, box plots of the half-maximal voltages for inactivation ($V_{0.5}$ inact.) and slopes (MOCK, n = 18; full-length PRRT2, n = 18; PRRT2ΔN, n = 16; PRRT2ΔC, n = 18). *F*, the time courses of the recovery from inactivation of peak currents at −20 mV are plotted on a semi-logarithmic scale for the four experimental conditions. *Inset:* Box plots of the plateau of recovery estimated from one-phase decay fit to the data (MOCK, n = 19; full-length PRRT2, n = 18; PRRT2ΔN, n = 17; PRRT2ΔC, n = 18). $p > 0.05$ *versus* MOCK. One-way ANOVA/Dunnett's test. *PRRT2*, proline-rich transmembrane protein 2.

also compared our Robetta model with the structures predicted by the AlphaFold2 and ESMFold programs (39, 40). The three configurations are very similar, showing the same succession of secondary structure patterns with almost identical numbers of helix turns. These results strengthen the validity of the model, which is presently the only structure available for the transmembrane PRRT2 region and is essential to investigate protein–protein interactions in atomic detail.

To define whether a single or both regions of PRRT2 are involved in interacting with Nav and modulating their biophysical properties, we generated NH₂- and COOH-terminal domain constructs and challenged them with Nav1.2 and Nav1.1 α-subunits to assess the extent and specificity of the interactions. PRRT2 fragments retained the subunit specificity of full-length PRRT2 and did not interact with Nav1.1 channels. Both PRRT2 deletion mutants bound to Nav1.2 α-subunits, although the NH₂-terminal region displayed a binding comparable to the full-length protein, suggesting an interaction with the cytoplasmic tails and/or intracellular loops of the Nav channel. However, in spite of the recapitulation of the binding activity and Nav channel specificity, the PRRT2 NH₂-terminal domain was unable to modulate the presence of active channels on the membrane and their biophysical properties.

On the contrary, the COOH-terminal region of PRRT2, whose stable intramembrane 3D structure was defined by MD simulations up to 1 μs simulation time (this paper) and fully

confirmed by the recently proposed AlphaFold2 and ESMFold algorithms (39, 40), binds to the channel about half of the full-length form, still preserving the selectivity for the Nav1.2 over the Nav1.1 α-subunit. The persistence of the binding indicates that in addition to cytosolic interactions, the intramembrane domain is another important site of PRRT2/Nav1.2 interaction. The functional importance of this interaction site is testified by the observation that the COOH-terminal region of PRRT2 could entirely recapitulate the effects of the full-length form both on current density (a functional measure of the membrane targeting), inactivation kinetics, and recovery from inactivation of the Nav1.2 channel. These observations restrict the functional effects to a PRRT2/Nav interplay within the plane of the membrane. Notwithstanding the very high homology between the transmembrane domains of Nav1.2 and Nav1.1 α-subunits, the COOH-terminal region of PRRT2 docks to the former and does not interact with the latter. This will open the way to further structural *in silico*, biochemical and electrophysiological investigations by performing site-directed mutagenesis of the nonconserved residues present in the voltage sensing and pore forming regions of the I-IV domains of Nav1.2, using the recently published optimized versions of Nav plasmids (42).

What is then the functional significance of the high intrinsic binding affinity of the cytosolic NH₂-terminal region of PRRT2? This region is rich in proline residues and displays an intrinsically disordered structure when analyzed by

AlphaFold2 ([1], [27], [39]). However, the significant binding of this PRRT2 region to Nav1.2 *versus* Nav1.1 contributes to the specificity of the interaction. It is possible that, upon binding to the cytosolic domains of Nav1.2, the NH_2-terminal region of PRRT2 gains a defined structure ([43]). The marked Nav1.2 binding activity coupled to the inability to modulate current density and biophysical properties of Nav1.2 channels is consistent with a model in which the NH_2-terminal intracellular domain may act as a Nav1.2 docking module, a PRRT2 "antenna" that favors the action of the intramembrane COOH-terminal domain on the plasma membrane exposure and biophysical properties ([Fig. 8]). The interaction between the NH_2-terminal domain of PRRT2 may be direct or mediated by Src-homology-3 domains binding to the proline-rich domain ([27]) or by the recently reported actin cytoskeleton interactions ([44], [45]).

In conclusion, the results support the high-order structure of the intramembrane COOH-terminal region of PRRT2 and indicate that intramembrane interactions with the transmembrane domains of Nav1.2 are responsible for the PRRT2 operated constraint of the membrane exposure of intracellular Nav1.2 channels and for decreasing the extent of activation of Nav1.2 channels by shifting the inactivation curve to more negative voltages and decreasing the extent of channel recovery from inactivation. The elucidation of the molecular bases of the inhibitory effects of PRRT2 on neuronal excitability is the first step toward a targeted therapeutic approach to PRRT2-linked paroxysmal diseases aimed at normalizing the intrinsic excitability of principal neurons without a generalized blockade of Nav channels that, although effective, is associated to unwanted side effects.

Experimental procedures

Plasmids

The human PRRT2-based constructs used in the study are the following: (i) PRRT2-HA, *i.e.*, pKH3-PRRT2-HA vector encoding for full-length PRRT2 with 3XHA tag fused at the COOH terminus ([27]); (ii) bacterial alkaline phosphatase (BAP)-HA, *i.e.,* pKH3-BAP-HA vector encoding for BAP with 3XHA tag fused at the COOH terminus ([31]); (iii) PRRT2ΔN-HA, *i.e.,* pKH3-PRRT2ΔN-HA encoding for the PRRT2 membrane domain (amino acids 261−340) with 3XHA tag fused at COOH terminus ([27]); (iv) PRRT2ΔC-HA, *i.e.*, pKH3-PRRT2ΔN-HA encoding for the PRRT2 cytosolic domain (amino acids 1−260) fused, for membrane targeting, to the second membrane domain of IFTM1(a kind gift of dr. Jacob S. Yount; RRID: Addgene_58415; ([45])). For the PRRT2ΔC-HA plasmid, the second membrane domain of IFTM1 was amplified by PCR from pCMV-HA-mIFITM1 with the following primers:

forward, ACGTAAGCTTACCGCCAAGTGCCTGAACAT

reverse, TCAGGTCGACTCTAATGGCACAGACAACG ATGAC and cloned in Hind3-Sal1 sites of the pKH3 plasmid (a kind gift of dr. Ian G. Macara, Addgene_12555; ([46])). The sequence corresponding to the cytosolic domain of PRRT2 (nucleotides: 1−780) was PCR amplified from pKH3-PRRT2-HA vector with the primers:
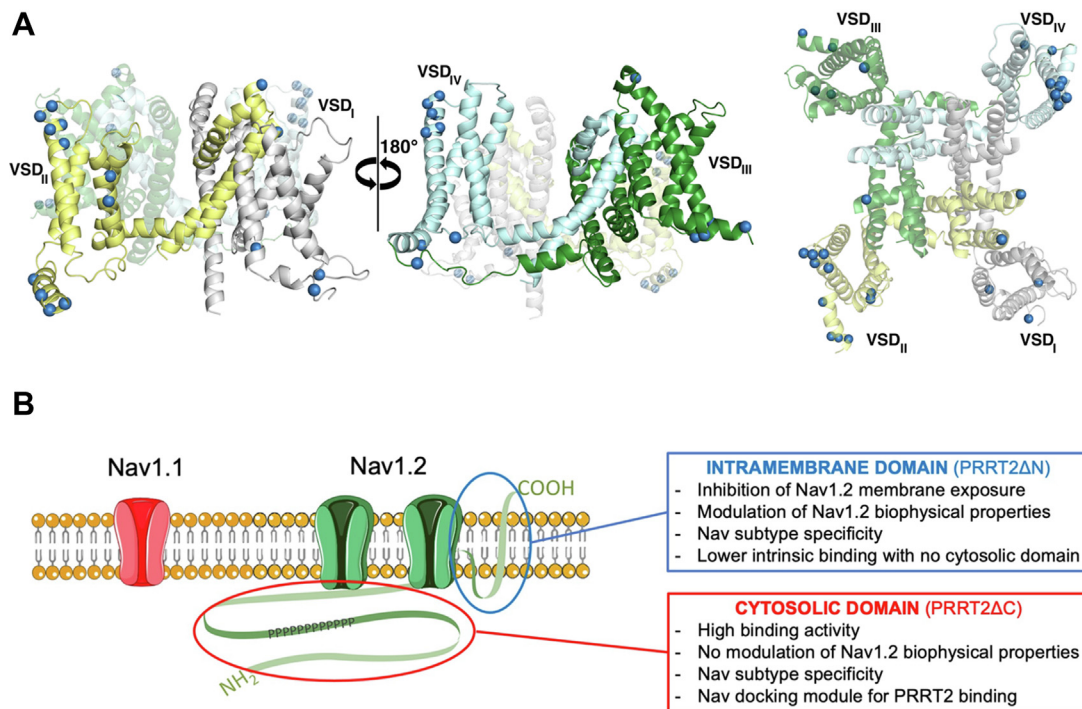
Figure 8. The tandem domain hypothesis of PRRT2-Nav1.2 specific interactions. *A*, structure of the transmembrane domains of the human Nav1.2 channel (PDB code: 6J8E; ([64])), lateral (*left*) and extracellular (*right*) view. Residues that differ with Nav1.1 are represented as *blue spheres*. *B*, schematic representation of the interactions between Nav1.2 and PRRT2. The NH_2-terminal intracellular domain may act as a Nav docking module favoring the action of the intramembrane COOH-terminal domain on the plasma membrane exposure and biophysical properties that are specific for Nav1.2. *PRRT2*, proline-rich transmembrane protein 2.

forward, CTGAAAGCTTATGGCAGCCAGCAGCTCTGA
GATC

reverse, GATCAAGCTTTTCACCCCCCTCCACCC-
CAGGA and cloned in Hind3 single site of the vector pKH3
encoding the second transmembrane domain of the previously
generated IFITM1 (47). The correct orientation and sequence
of the cloned fragment were controlled by restriction analysis
followed by DNA sequencing.

Live and conventional cell immunolabeling

Hek-Na$_V$1.2 cells transfected with PRRT2-HA, PRRT2ΔC-
HA, or PRRT2ΔN-HA constructs were live labeled by diluting
primary antibodies (mouse anti-HA, 1:500, Millipore) in cul-
ture medium for 30 min at 37 °C/5% CO$_2$ to detect surface
epitopes, followed by fixation with 4% paraformaldehyde and
incubation with Alexa Fluor-594 secondary antibodies. After
several washes in phosphate-buffered saline (PBS), coverslips
were mounted using Prolong Gold antifade reagent (Invi-
trogen) containing 4′,6′-diamidino-2-phenylindole for nuclear
staining. Hek-Nav1.2 cells transfected with PRRT2-HA,
PRRT2ΔC-HA or PRRT2ΔN-HA constructs were fixed in 4%
paraformaldehyde at room temperature for 20 min, washed in
PBS, and blocked with 10% bovine serum albumin (BSA) for
20 min. Samples were sequentially incubated with mouse anti-
pan-Nav (Sigma; 1:100 in 5% BSA) and rabbit anti-HA,
(Invitrogen; 1:500 in 5% BSA) primary antibodies, followed
by Alexa 564-conjugated or 488-conjugated secondary anti-
bodies (Invitrogen; 1:200 in 5% BSA) at room temperature.
After several washes in PBS, coverslips were mounted using
Prolong Gold antifade reagent (Invitrogen) containing 4′,6′-
diamidino-2-phenylindole for nuclear staining.

Cell cultures and transfection

Hek293 cells stably expressing human Nav1.2 or Nav1.1
were kind gifts from Drs. Enzo Wanke and Marzia Lecchi
(Milano-Bicocca University). To map the PRRT2/Nav in-
teractions, Hek-Nav cells were transiently transfected with the
empty pKH3 vector (MOCK), BAP-HA, full-length PRRT2-
HA, or its deletion mutants PRRT2ΔN-HA and PRRT2ΔC-
HA. All Hek293 cell lines were maintained in DMEM/F12
(1:1) supplemented with 10% fetal bovine serum, 100 U/ml
penicillin, 100 μg/ml streptomycin and, for selection of stable
Nav clones, 500 μg/ml G418. Cell lines were transfected with
2 μg of each plasmid according to the manufacturer's recom-
mendations at 70% confluency using Lipofectamine 2000. All
reagents were purchased from ThermoFisher Scientific. To
identify transfected cells for electrophysiology, the reporter
EGFP was co-transfected. Transfected cells were dissociated,
re-plated at low density about 24 h posttransfection and
recorded after other 24 h.

Pull-down assays

Naïve Hek293 cells expressing the PRRT2 variants were
harvested in lysis buffer (150 mM NaCl, 50 mM Tris, 1 mM
EDTA and 1% Triton X-100 supplemented with protease in-
hibitor cocktail) 48 h after transfection and centrifuged at

10,000g for 10 min at 4 °C. Kept an aliquot for input, the
supernatant was incubated with 50 μl of monoclonal anti-HA-
agarose affinity beads (Sigma-Aldrich) for 2 h at 4 °C. After
three washes in lysis buffer, the beads were incubated with cell
extracts from Hek293 cells expressing either Nav1.2 or Nav1.1
for 2 h at 4 °C. After extensive washes in lysis buffer and
detergent-free lysis buffer, samples were resolved by sodium
dodecyl sulfate polyacrylamide gel electrophoresis and sub-
jected to Western blotting with pan-Nav (1:300, Sigma-Aldrich
Cat.S8809, RRID:AB_477552) and HA (1:1000, Thermo Fisher
Scientific Cat.71–5500, RRID:AB_2533988) specific antibodies.
Actin immunoreactivity (anti-actin antibody 1:1000, Sigma-
Aldrich Cat.A4700, RRID:AB_476730) was used as control of
equal loading.

Western blotting

For Western blotting analysis, samples were subjected to
sodium dodecyl sulfate polyacrylamide gel electrophoresis af-
ter 5-min heating at 50 °C and blotted onto nitrocellulose
membranes (Whatman). Blotted membranes were blocked for
1 h in 5% milk in Tris-buffered saline (10 mM Tris, 150 mM
NaCl, pH 8.0) plus 0.1% Triton X-100 and incubated overnight
at 4 °C with the appropriate primary antibody. Membranes
were washed and incubated at room temperature for 1 h with
peroxidase-conjugated secondary antibodies. The proteins of
interest were revealed with the ECL chemiluminescence
detection system (Bio-Rad).

Patch-clamp recordings

Patch pipettes prepared from thin-borosilicate glass (Hil-
genberg) were pulled and fire-polished to a final resistance of 2
to 4 MΩ when filled with standard internal solution. Whole-
cell currents were recorded using an EPC-10 amplifier
(HEKA Electronic). Recordings with leak currents >200 pA or
series resistance (R$_s$) >10 MΩ were discarded. Data acquisition
was performed using PatchMaster program (HEKA Elek-
tronic). R$_s$ was compensated 80% (2 μs response time), and the
compensation was checked and eventually readjusted before
each stimulation protocol. No significant differences in average
uncompensated R$_s$ errors were found in the cells belonging to
the four experimental groups. All recordings were performed
at 22 to 24 °C. Voltage-clamp recordings of voltage-gated Na$^+$
currents were performed using the following solutions:
extracellular (in mM): 140 NaCl, 3 KCl, 1 MgCl$_2$, 1 CaCl$_2$, 10
Hepes, 10 Mannitol (pH 7.3 with NaOH); intracellular (in
mM): 140 CsCl, 10 NaCl, 2 EGTA, 10 Hepes (pH 7.3 with
CsOH). Whole-cell family currents of fast inactivating Nav
channels were evoked by 5 mV steps depolarization from –80
to 40 mV, and cells were held at –100 mV. Steady-state
inactivation curves were constructed by recording the peak
currents amplitude evoked by 20-ms test pulses to –10 mV
after 500-ms pre-pulses to potentials over the range of –130 to
20 mV. The Na$^+$ current density (J) was obtained by dividing
the peak inward current by the cell capacitance (nA/pF). The
conductance/voltage relationship (G-V) curves were obtained
by converting the maximal current values, evoked with the

voltage step protocols, to conductance using the relation $G_{Na} = I_{Na}/(V-E_{Na})$, where G_{Na} is the Na⁺ conductance, I_{Na} is the peak Na⁺ current, V is the command pulse potential, and E_{Na} is the theoretical reversal potential of Na⁺ current calculated by Nernst equation. G-V curves were normalized and fitted with the Boltzmann function $G/G_{max} = 1/(1 + \exp[(V - V_{1/2})/k])$, where G is the conductance, G_{max} is the maximal conductance, $V_{1/2}$ is the half-maximal voltage of activation, and k is the slope factor. Inactivation curves were fitted with the Boltzmann equation in the following form: $1/[1 + \exp(V_{1/2} - V)/k]$. Time-dependent rate of recovery from inactivation was calculated by prepulsing the cell with a 20-ms step to –20 mV to inactivate Na⁺ channels and then bringing back the potential to –100 mV for increasing recovery durations (0.5, 1, 2, 4, 8, 32, 64, 128, and 256 ms) before the test pulse of –20 mV. Time constants for recovery from inactivation were calculated by fitting data from each recorded cell to a first order exponential function and averaging time constants across cells. To minimize space-clamp problems, we recoded only isolated transfected cells with a soma diameter of about <30 μm. Membrane capacitance artifacts and leakage currents were eliminated by P/N leak subtraction procedure. For all electrophysiological experiments, data acquisition was performed using PatchMaster programs (HEKA Elektronic).

Structural models

Our first model structure of the PRRT2 transmembrane domain (sequence G261 to K340) was generated by Rossi *et al.* (27) using the Robetta (48) server, which uses the Rosetta software (49) to predict models of protein domains by combining template-based homology modeling and *de novo* approaches. Two additional models of the same protein segment were generated using AlphaFold2 (39) and ESMFold (40).

MD simulations

MD simulations were performed using NAMD3.0 (50) with the all-atom CHARMM36m force field (51, 52). The membrane builder application of the CHARMM-GUI server (53, 54) was used for the preparation of all the input files. The Robetta model was oriented with the PPM web server (55), inserted into a 1-palmitoyl-2-oleoyl-sn-glycero-3-phosphocholine lipid bilayer and solvated with water molecules, using the TIP3P model (56). Na⁺ and Cl⁻ ions were added to neutralize the total system charge at a physiological concentration of 0.15 M. The whole system counted 108,608 atoms in a rectangular box. Periodic boundary conditions were applied to replicate the system and remove box surface effects, and the particle mesh Ewald method was used for long-range electrostatics (57), with a grid spacing of 1 Å and sixth-order B-splines. A cut-off of 12 Å and smooth switching at 10 Å was used for Lennard–Jones interactions. Chemical bond distances involving hydrogen atoms were constrained using the SHAKE/RATTLE algorithm (58). Before production, the system was energy minimized, and later, it was equilibrated by running a 15 ns-long simulation in the isobaric-isothermal ensemble, NpT, with N total number of atoms, P = 1 atm and T = 310 K, using positional restraints on the protein atoms. Subsequently, two independent 1 μs-long MD simulations were produced in the NPT ensemble at the same temperature and pressure maintained by a Langevin thermostat and Nosé-Hoover Langevin piston pressure control (59). A timestep of 2 fs was employed for one replica, while the hydrogen mass repartitioning method (HMR) (60) was employed to allow the use of a 4 fs timestep for the second one (61). The MD trajectories were inspected and analyzed to validate the structural stability of the PRRT2 protein using VMD (62) and PyMOL (63). Alpha carbon root mean square deviation and cross-distances analysis were performed for PRRT2 replicas trajectories through tcl scripting (62).

Statistical analysis

Experimental data are expressed as box plots for the number of independent preparations detailed in the figure legends. The box plots elements are the following: center line, median (Q2); box limits, 25th (Q1)-75th (Q3) percentiles; whiskers, min to max values. Normal distribution of data was assessed using the D'Agostino-Pearson's normality test. To compare more than two normally distributed sample groups, one-way ANOVA, followed by *post hoc* multiple comparison tests was used. In cases in which data were not normally distributed, nonparametric one-way ANOVA (Kruskal–Wallis' test) followed by the Dunn's multiple comparison test was used. Alpha levels for all tests were 0.05% (95% confidence intervals). Statistical analysis was carried out using Prism (GraphPad Software, Inc.) software. In addition to the box plots, data are summarized as means ± SD for the interactions of PRRT2 with Nav1.2 and Nav1.1 in Tables S1 and S2, respectively. The exact *p* values from the statistical analyses are reported in Table S3.

Data availability

The datasets generated and/or analyzed in the current study are available from the corresponding author on reasonable request.

Abbreviations—The abbreviations used are: BAP, bacterial alkaline phosphatase; IC, infantile convulsions; IFITM1, interferon-induced transmembrane protein 1; MD, molecular dynamics; PRRT2, proline-rich transmembrane protein 2; PKD, paroxysmal kinesigenic dyskinesia; PBS, phosphate-buffered saline; PRRT2ΔN, COOH-terminal PRRT2; PRRT2ΔC, NH$_2$-terminal PRRT2.

References

1. Chen, W.-J., Lin, Y., Xiong, Z.-Q., Wei, W., Ni, W., Tan, G.-H., *et al.* (2011) Exome sequencing identifies truncating mutations in PRRT2 that cause paroxysmal kinesigenic dyskinesia. *Nat. Genet.* **43**, 1252–1255

2. Lee, H. Y., Huang, Y., Bruneau, N., Roll, P., Roberson, E. D., Hermann, M., *et al.* (2012) Mutations in the gene PRRT2 cause paroxysmal kinesigenic dyskinesia with infantile convulsions. *Cell Rep.* **1**, 2–12

3. Ebrahimi-Fakhari, D., Saffari, A., Westenberger, A., and Klein, C. (2015) The evolving spectrum of PRRT2-associated paroxysmal diseases. *Brain* **138**, 3476–3495

4. Gardiner, A. R., Jaffer, F., Dale, R. C., Labrum, R., Erro, R., Meyer, E., *et al.* (2015) The clinical and genetic heterogeneity of paroxysmal dyskinesias. *Brain* **138**, 3567–3580

5. Heron, S. E., and Dibbens, L. M. (2013) Role of PRRT2 in common paroxysmal neurological disorders: a gene with remarkable pleiotropy. *J. Med. Genet.* **50**, 133–139

6. Valtorta, F., Benfenati, F., Zara, F., and Meldolesi, J. (2016) PRRT2: from paroxysmal disorders to regulation of synaptic function. *Trends Neurosci.* **39**, 668–679

7. Döring, J. H., Saffari, A., Bast, T., Brockmann, K., Ehrhardt, L., Fazeli, W., *et al.* (2020) The phenotypic spectrum of PRRT2-associated paroxysmal neurologic disorders in childhood. *Biomedicines* **8**, 456

8. Balagura, G., Riva, A., Marchese, F., Iacomino, M., Madia, F., Giacomini, T., *et al.* (2020) Clinical spectrum and genotype-phenotype correlations in PRRT2 Italian patients. *Eur. J. Paediatr. Neurol.* **28**, 193–197

9. Pan, Y., Liu, Q., Zhang, J., Yang, Y., Tian, Y., Zeng, J., *et al.* (2020) PRRT2 frameshift mutation reduces its mRNA stability resulting loss of function in paroxysmal kinesigenic dyskinesia. *Biochem. Biophys. Res. Commun.* **522**, 553–559

10. Wu, L., Tang, H. D., Huang, X. J., Zheng, L., Liu, X. L., Wang, T., *et al.* (2014) PRRT2 truncated mutations lead to nonsense-mediated mRNA decay in Paroxysmal Kinesigenic Dyskinesia. *Parkinsonism Relat. Disord.* **20**, 1399–1404

11. Liu, Y. T., Nian, F. S., Chou, W. J., Tai, C. Y., Kwan, S. Y., Chen, C., *et al.* (2016) PRRT2 mutations lead to neuronal dysfunction and neurodevelopmental defects. *Oncotarget* **7**, 39184–39196

12. Tsai, M. H., Nian, F. S., Hsu, M. H., Liu, W. S., Liu, Y. T., Liu, C., *et al.* (2019) PRRT2 missense mutations cluster near C-terminus and frequently lead to protein mislocalization. *Epilepsia* **60**, 807–817

13. Delcourt, M., Riant, F., Mancini, J., Milh, M., Navarro, V., Roze, E., *et al.* (2015) Severe phenotypic spectrum of biallelic mutations in PRRT2 gene. *J. Neurol. Neurosurg. Psych.* **86**, 782–785

14. Huang, X. J., Wang, T., Wang, J. L., Liu, X. L., Che, X. Q., Li, J., *et al.* (2015) Paroxysmal kinesigenic dyskinesia: clinical and genetic analyses of 110 patients. *Neurology* **85**, 1546–1553

15. Labate, A., Tarantino, P., Viri, M., Mumoli, L., Gagliardi, M., Romeo, A., *et al.* (2012) Homozygous c.649dupC mutation in PRRT2 worsens the BFIS/PKD phenotype with mental retardation, episodic ataxia, and absences. *Epilepsia* **53**, e196–e199

16. Michetti, C., Corradi, A., and Benfenati, F. (2017) PRRT2, a network stability gene. *Oncotarget* **8**, 55770–55771

17. Lerche, H. (2018) Synaptic or ion channel modifier? PRRT2 is a chameleon-like regulator of neuronal excitability. *Brain* **141**, 938–941

18. Michetti, C., Castroflorio, E., Marchionni, I., Forte, N., Sterlini, B., Binda, F., *et al.* (2017) The PRRT2 knockout mouse recapitulates the neurological diseases associated with PRRT2 mutations. *Neurobiol. Dis.* **99**, 66–83

19. Tan, G. H., Liu, Y. Y., Wang, L., Li, K., Zhang, Z. Q., Li, H. F., *et al.* (2018) PRRT2 deficiency induces paroxysmal kinesigenic dyskinesia by regulating synaptic transmission in cerebellum. *Cell Res.* **28**, 90–110

20. Mo, J., Wang, B., Zhu, X., Wu, X., and Liu, Y. (2019) PRRT2 deficiency induces paroxysmal kinesigenic dyskinesia by influencing synaptic function in the primary motor cortex of rats. *Neurobiol. Dis.* **121**, 274–285

21. Valente, P., Romei, A., Fadda, M., Sterlini, B., Lonardoni, D., Forte, N., *et al.* (2019) Constitutive inactivation of the PRRT2 gene alters short-term synaptic plasticity and promotes network hyperexcitability in hippocampal neurons. *Cereb. Cortex* **29**, 2010–2033

22. Calame, D. J., Xiao, J., Khan, M. M., Hollingsworth, T. J., Xue, Y., Person, A. L., *et al.* (2020) Presynaptic PRRT2 deficiency causes cerebellar dysfunction and paroxysmal kinesigenic dyskinesia. *Neuroscience* **448**, 272–286

23. Sterlini, B., Romei, A., Parodi, C., Aprile, D., Oneto, M., Aperia, A., *et al.* (2021) An interaction between PRRT2 and Na⁺/K⁺ ATPase contributes to the control of neuronal excitability. *Cell Death Dis.* **12**, 292

24. Binda, F., Valente, P., Marte, A., Baldelli, P., and Benfenati, F. (2021) Increased responsiveness at the cerebellar input stage in the PRRT2 knockout model of paroxysmal kinesigenic dyskinesia. *Neurobiol. Dis.* **152**, 105275

25. Lu, B., Lou, S. S., Xu, R. S., Kong, D. L., Wu, R. J., Zhang, J., *et al.* (2021) Cerebellar spreading depolarization mediates paroxysmal movement disorder. *Cell Rep.* **36**, 109743

26. Forrest, M. P., Dos Santos, M., Piguel, N. H., Wang, Y.-Z., Hawkins, N. A., Bagchi, V. A., *et al.* (2023) Rescue of neuropsychiatric phenotypes in a mouse model of 16p11.2 duplication syndrome by genetic correction of an epilepsy network hub. *Nat. Commun.* **14**, 825

27. Rossi, P., Sterlini, B., Castroflorio, E., Marte, A., Onofri, F., Valtorta, F., *et al.* (2016) A novel topology of proline-rich transmembrane protein 2 (PRRT2): hints for an intracellular function at the synapse. *J. Biol. Chem.* **291**, 6111–6123

28. Valente, P., Castroflorio, E., Rossi, P., Fadda, M., Sterlini, B., Cervigni, R. I., *et al.* (2016) PRRT2 is a key component of the Ca²⁺-dependent neurotransmitter release machinery. *Cell Rep.* **15**, 117–131

29. Coleman, J., Jouannot, O., Ramakrishnan, S. K., Zanetti, M. N., Wang, J., Salpietro, V., *et al.* (2018) PRRT2 regulates synaptic fusion by directly modulating SNARE complex assembly. *Cell Rep.* **22**, 820–831

30. Ferrante, D., Sterlini, B., Prestigio, C., Marte, A., Corradi, A., Onofri, F., *et al.* (2021) PRRT2 modulates presynaptic Ca²⁺ influx by interacting with P/Q-type channels. *Cell Rep.* **35**, 109248

31. Fruscione, F., Valente, P., Sterlini, B., Romei, A., Baldassari, S., Fadda, M., *et al.* (2018) PRRT2 controls neuronal excitability by negatively modulating Na⁺ channel 1.2/1.6 activity. *Brain* **141**, 1000–1016

32. Catterall, W. A., Lenaeus, M. J., and Gamal El-Din, T. M. (2020) Structure and pharmacology of voltage-gated sodium and calcium channels. *Annu. Rev. Pharmacol. Toxicol.* **60**, 133–154

33. Guerrini, R., Conti, V., Mantegazza, M., Balestrini, S., Galanopoulou, A. S., and Benfenati, F. (2022) Developmental and epileptic

encephalopathies: From genetic heterogeneity to phenotypic continuum. *Physiol. Rev.* **103**, 433–513

34. Valente, P., Marte, A., Franchi, F., Sterlini, B., Casagrande, S., Corradi, A., *et al.* (2022) A push-pull mechanism between PRRT2 and β4-subunit differentially regulates membrane exposure and biophysical properties of Na$_V$1.2 sodium channels. *Mol. Neurobiol.* https://doi.org/10.1007/s12035-022-03112-x

35. Döring, J. H., Saffari, A., Bast, T., Brockmann, K., Ehrhardt, L., Fazeli, W., *et al.* (2022) Efficacy, tolerability, and retention of antiseizure medications in prrt2-associated infantile epilepsy. *Neurol. Genet.* **8**, e200020

36. Dale, R. C., Gardiner, A., Branson, J. A., and Houlden, H. (2014) Benefit of carbamazepine in a patient with hemiplegic migraine associated with PRRT2 mutation. *Dev. Med. Child Neurol.* **56**, 910

37. Chou, I. C., Lin, S. S., Lin, W. D., Wang, C. H., Chang, Y. T., Tsai, F. J., *et al.* (2014) Successful control with carbamazepine of family with paroxysmal kinesigenic dyskinesia of PRRT2 mutation. *Biomedicine (Taipei)* **4**, 15

38. Weston, S., Czieso, S., White, I. J., Smith, S. E., Kellam, P., and Marsh, M. (2014) A membrane topology model for human interferon inducible transmembrane protein 1. *PLoS One* **9**, e104341

39. Jumper, J., Evans, R., Pritzel, A., Green, T., Figurnov, M., Ronneberger, O., *et al.* (2021) Highly accurate protein structure prediction with AlphaFold. *Nature* **596**, 583–589

40. Rives, A., Meier, J., Sercu, T., Goyal, S., Lin, Z., Liu, J., *et al.* (2021) Biological structure and function emerge from scaling unsupervised learning to 250 million protein sequences. *Proc. Natl. Acad. Sci. U. S. A.* **118**, e2016239118

41. Winters, J. J., and Isom, L. L. (2016) Developmental and regulatory functions of Na⁺ channel non-pore-forming β subunits. *Curr. Top Membr.* **78**, 315–351

42. DeKeyser, J. M., Thompson, C. H., and George, A. L., Jr. (2021) Cryptic prokaryotic promoters explain instability of recombinant neuronal sodium channels in bacteria. *J. Biol. Chem.* **296**, 100298

43. Ithuralde, R. E., Roitberg, A. E., and Turjanski, A. G. (2016) Structured and unstructured binding of an intrinsically disordered protein as revealed by atomistic simulations. *J. Am. Chem. Soc.* **138**, 8742–8751

44. Savino, E., Cervigni, R. I., Povolo, M., Stefanetti, A., Ferrante, D., Valente, P., *et al.* (2020) Proline-rich transmembrane protein 2 (PRRT2) regulates the actin cytoskeleton during synaptogenesis. *Cell Death Dis.* **11**, 856

45. Savino, E., Guarnieri, F. C., Tsai, J. W., Corradi, A., Benfenati, F., and Valtorta, F. (2021) An emerging role of PRRT2 in regulating growth cone morphology. *Cells* **10**, 2666

46. Mattingly, R. R., and Macara, I. G. (1996) Phosphorylation-dependent activation of the Ras-GRF/CDC25Mm exchange factor by muscarinic receptors and G-protein beta gamma subunits. *Nature* **82**, 268–272

47. Hach, J. C., McMichael, T., Chesarino, N. M., and Yount, J. S. (2013) Palmitoylation on conserved and nonconserved cysteines of murine IFITM1 regulates its stability and anti-influenza A virus activity. *J. Virol.* **87**, 9923–9927

48. Chivian, D., Kim, D. E., Malmström, L., Bradley, P., Robertson, T., Murphy, P., *et al.* (2003) Automated prediction of CASP-5 structures using the Robetta server. *Proteins* **53**, 524–533

49. Leaver-Fay, A., Tyka, M., Lewis, S. M., Lange, O. F., Thompson, J., Jacak, R., *et al.* (2011) ROSETTA3: an object-oriented software suite for the simulation and design of macromolecules. *Met. Enzymol.* **487**, 545–574

50. Phillips, J. C., Hardy, D. J., Maia, J. D., Stone, J., Ribeiro, J. V., Bernardi, R. C., *et al.* (2020) Scalable molecular dynamics on CPU and GPU architectures with NAMD. *J. Chem. Phys.* **153**, 044130

51. Brooks, B. R., Brooks, C. L., 3rd, Mackerell, A. D., Jr., Nilsson, L., Petrella, R. J., Roux, B., *et al.* (2009) Charmm: the biomolecular simulation program. *J. Comput. Chem.* **30**, 1545–1614

52. Huang, J., Rauscher, S., Nawrocki, G., Ran, T., Feig, M., de Groot, B., *et al.* (2017) CHARMM36: an improved force field for folded and intrinsically disordered proteins. *Biophys. J.* **112**, 175a–176a

53. Jo, S., Kim, T., Lyer, V. G., and Im, W. (2008) CHARMM-GUI: a web-based graphical user interface for CHARMM. *J. Comput. Chem.* **29**, 1859–1865

54. Lee, J., Cheng, X., Swails, J. M., Yeom, M. S., Eastman, P. K., Lemkul, J. A., *et al.* (2016) CHARMM-GUI input generator for NAMD, GROMACS, AMBER, OpenMM, and CHARMM/OpenMM simulations using the CHARMM36 additive force field. *J. Chem. Theor. Comput.* **12**, 405–413

55. Lomize, M. A., Pogozheva, I. D., Joo, H., Mosberg, H. I., and Lomize, A. L. (2012) OPM database and PPM web server: resources for positioning of proteins in membranes. *Nucl. Acids Res.* **40**, D370–D376

56. Neria, E., Fischer, S., and Karplus, M. (1996) Simulation of activation free energies in molecular systems. *J. Chem. Phys.* **105**, 1902–1921

57. Darden, T., York, D., and Pedersen, L. (1993) Particle mesh Ewald: an N-log(N) method for Ewald sums in large systems. *J. Chem. Phys.* **98**, 10089–10092

58. Ryckaert, J. P., Ciccotti, G., and Berendsen, H. J. C. (1977) Numerical integration of the Cartesian equations of motion of a system with constraints: molecular dynamics of n-alkanes. *J. Comput. Phys.* **23**, 327–341

59. Feller, S. E., Zhang, Y., Pastor, R. W., and Brooks, B. R. (1995) Constant pressure molecular dynamics simulation: the Langevin piston method. *J. Chem. Phys.* **103**, 11

60. Hopkins, C., Le Grand, S., Walker, R., and Roitberg, A. (2015) Long-time-step molecular dynamics through hydrogen mass repartitioning. *J. Chem. Theor. Comput.* **11**, 1864–1874

61. Balusek, C., Hwang, H., Lau, C. H., Lundquist, K., Hazel, A., Pavlova, A., *et al.* (2019) Accelerating membrane simulations with hydrogen mass repartitioning. *J. Chem. Theor. Comput.* **15**, 4673–4686

62. Humphrey, W., Dalke, A., and Schulten, K. (1996) Vmd - visual molecular dynamics. *J. Mol. Graphics* **14**, 33–38

63. *The PyMOL Molecular Graphics System, Version 2.0.* (2002). Schrödinger, LLC, New York, NY

64. Pan, X., Li, Z., Huang, X., Huang, G., Gao, S., Shen, H., *et al.* (2019) Molecular basis for pore blockade of human Na⁺ channel Na$_V$1.2 by the μ-conotoxin KIIIA. *Science* **363**, 1309–1313